Ceramics International 51 (2025) 63441–63452

Contents lists available at ScienceDirect

Ceramics International

journal homepage: www.elsevier.com/locate/ceramint

Thermal and chemical parameters controlling phase stability and caesium immobilisation in phosphate-based geopolymers, using a chabazite-rich volcanic tuff

Fabio Fattori [a,*], Gabriele Magugliani [a], Giuseppe Marinelli [a], Davide Comboni [b], Giacomo Diego Gatta [b], Alessandro Girella [c], Chiara Milanese [c], Andrea Santi [a], Francesco Galluccio [a], Ilaria Moschetti [a], Simona Šandalová [a], Elena Macerata [a], Mario Mariani [a], Eros Mossini [a]

[a] Politecnico di Milano, Department of Energy, Piazza Leonardo da Vinci, 32, 20133, Milano, Italy
[b] Università degli Studi di Milano, Department of Earth Sciences, Via Sandro Botticelli, 23, 20133, Milano, Italy
[c] Università di Pavia, Department of Chemistry and C.S.G.I., Viale Taramelli 16, 27100, Pavia, Italy

ARTICLE INFO

Keywords:
Phosphate-based geopolymers
Radioactive waste management
Caesium leaching
Zeolite chabazite

ABSTRACT

Acid-activated phosphate-based geopolymers emerged as alternatives to Portland cement thanks to their promising mechanical and thermal properties, as well as their potential for the solidification/stabilisation of hazardous wastes. In this regard, a peculiar application field can be found in radioactive waste management operations, where the immobilisation of radionuclides is one of the primary objectives. However, limited knowledge is available regarding the effectiveness of this kind of binders in this context. This study investigated the use of a natural, chabazite-rich, volcanic tuff as a novel precursor for phosphate-based geopolymers in radioactive waste management applications. The effects of the phosphoric acid concentration and the curing temperature on the geopolymerisation process were assessed. Elemental dissolution tests were used to estimate the release of aluminium, silicon, and iron from the volcanic tuff, showing extensive aluminium release due to the instability of chabazite in acid environments. The mineralogical and microstructural evolution of the samples was examined via quantitative phase analysis by X-ray diffraction and scanning electron microscopy, confirming chabazite dissolution and the subsequent formation of crystalline taranakite phase primarily governed by phosphoric acid concentration. Caesium retention, a key requirement for radioactive waste conditioning, was assessed through leaching tests. All samples demonstrated excellent caesium immobilisation capabilities, outperforming traditional cementitious matrices and comparable to alkali-activated geopolymers. The samples also met the Italian waste acceptance criterion for radioactive waste disposal. Therefore, chabazite-rich volcanic tuff can serve as a viable, natural precursor for phosphate-based geopolymers, providing a lower-impact alternative to other commonly used precursors.

1. Introduction

In recent years, geopolymers (GPs) emerged as promising candidates for cement substitution thanks to their high engineering performances and a more favourable environmental footprint. These materials are obtained by mixing a source of amorphous aluminosilicates, called *precursors*, and an *activator*, which can be an alkaline or acidic solution. The extreme pH conditions promote the dissolution of the precursors, thus releasing silicon and aluminium species which subsequently react and reorganise, forming 3D networks made by (−Si−O−Al−) and (−Si−O−Si−) building units [1,2]. GPs typically have a better environmental footprint compared to cement due to their reduced energy demand and lower reliance on virgin raw materials [3,4]. In fact, common GP precursors are industrial byproducts such as coal fly ash, ground granulated blast furnace slag, red mud, and rice husk ash, all playing an important role in terms of material repurposing and circular economy [5]. Moreover, natural materials such as (meta)kaolin, zeolites, and volcanic ash can be used requiring less energy-intensive

* Corresponding author.
E-mail address: fabio.fattori@polimi.it (F. Fattori).

https://doi.org/10.1016/j.ceramint.2025.11.131
Received 25 July 2025; Received in revised form 5 November 2025; Accepted 10 November 2025
Available online 11 November 2025

processing compared to clinker production [6].

Other than applications in the building sector, GPs were successfully proposed for the conditioning of low-to-intermediate level radioactive waste (RW). The confinement and immobilisation of radioactive contaminants inside proper conditioning matrices must be a priority to avoid potential releases into the environment, which may affect both humans and the biosphere [7,8]. In particular, GPs can overcome the incompatibilities of challenging RWs with conventional cementitious matrices, as in the case of liquid or solid organic waste, and borate- or sulphate-rich wastes, allowing elevated loading factors and thus substantial economical savings [9–11]. Caesium, a highly abundant and mobile fission product commonly found in RW as short-lived Cs-137 and long-lived Cs-135, is often selected as a representative of radioactive contamination, and its diffusion and release from conditioning matrices is employed as a metric to evaluate their immobilisation effectiveness. In this regard, alkali-activated GPs have proven to be effective for RW conditioning through low diffusion coefficients. This can be explained by the three-dimensional cage-like framework of these binders, similar to the ones of zeolites, which determines their selectivity for specific cations [12,13]. Conversely, conventional cementitious matrices have a low caesium encapsulation and confinement capacity, particularly during the hydration phase, limiting their effectiveness and reliability within RW management [14].

Although less investigated, acid-activated phosphate-based geopolymers (PGPs) can offer several advantages over their alkali-activated counterparts, mainly in terms of mechanical resistance and thermal stability [1]. Moreover, PGPs exhibit elevated sorption capacity particularly towards anionic species thanks to their positive surface charge, contrarily to the negatively charged surface of alkali-activated GP [15,16]. Although preliminary research hinted that PGPs can also effectively immobilise, under certain conditions, problematic cations, for example heavy metals (in their ionic form) such as Pb^{2+}, or fission (Cs^{+} and Sr^{2+}) and activation (Co^{2+}) products, further investigation is needed [17–19].

The main activator investigated in literature is phosphoric acid, though alternatives such as aluminium and potassium dihydrogen phosphate might also be used [20,21]. Both the curing temperature and the activator concentration deeply influence the properties of the PGPs. When the activator concentration is too low, the dissolution of the precursors is hindered and the formation of the PGP network is inhibited, resulting in poor mechanical properties. Conversely, excessive amounts of activator may lead to unreacted phosphate species and higher grout viscosity; both these factors negatively affect mechanical properties and excessively extend the setting times [22–24]. Curing temperatures above 20 °C enhance the dissolution rate of aluminium, which is the dominant factor influencing the geopolymerisation reaction kinetics of PGPs, thereby reducing the setting time and improving mechanical strength. However, excessive temperatures (indicatively above 80 °C) can lead to the formation of cracks or disrupt the geopolymerisation process, thus reducing mechanical performances [25,26]. While these parameters are clearly dependent on the properties of the raw materials, e.g. the precursor type and its particle size distribution, most literature studies suggest that optimal mechanical properties can be achieved with a phosphoric acid concentration of approximately 8–10 mol/L and a curing temperature of about 40–60 °C [25–27].

Further investigation is, however, needed to validate these findings for a broader range of precursors, as most studies focused only on metakaolin and fly ash [1]. Chabazite-rich volcanic tuff (VT) is a promising natural precursor for GP synthesis, as it requires minimal processing, mostly limited to extraction and grinding. The use of this material in alkali-activated GPs has already been demonstrated to inhibit leaching of Cs, as chabazite is one of the most selective zeolites for Cs [10,11]. The working hypothesis of this study is that the high chabazite content in the investigated VT might not only participate in the geopolymerisation process, but it can additionally play a key role in enhancing Cs immobilisation within the PGP matrix. Such a precursor, to the best of authors' knowledge, has not yet been investigated for PGPs. A previous work by *Baykara* et al. investigated the properties and the excellent environmental impact of natural Ecuadorian zeolite tuff-based PGPs [28]. The VT proposed in this study, however, differs substantially from the one proposed in the aforementioned work in terms of mineralogy, elemental composition, and granulometry [28]. Furthermore, the high concentration of zeolite chabazite in this VT (about 65 % w/w) makes this material particularly interesting for its expected Cs immobilisation [29–31].

The aim of this work was to evaluate the interaction between phosphoric acid and the chabazite-rich VT, investigating its mineralogical evolution and Cs retention efficacy under an acidic environment. Therefore, PGP samples were prepared using phosphoric acid solutions at varying concentrations. The effect of thermal curing at various temperatures up to 60 °C was also assessed. A thorough phase composition and microstructural characterisation of the samples was also performed to ascertain the effects of the activator concentration and curing temperature, employing techniques such as powder Quantitative Phase Analysis by X-Ray Diffraction (QPA-XRD) and Scanning Electron Microscopy (SEM). The aluminium release from VT in phosphoric acid solutions was measured for all combinations of acid concentrations and temperatures to analyse the de-alumination process kinetics and corroborate experimental findings. The dissolution of silicon and iron, two other relevant elements for PGPs, was also investigated. Finally, the Cs leaching resistance of the samples was evaluated, as it is a key requirement outlined by the Waste Acceptance Criterion (WAC) established by national regulatory bodies for conditioned RWs.

2. Material and methods

2.1. Raw materials and sample preparation

The micronised chabazite-rich VT (Zeolite Fertenia™, Fertenia S.r.l.) used in this study has already been characterised by *Santi* et al. [10]. This VT is mainly composed of SiO_2 (52 %[1]), Al_2O_3 (17 %), CaO (6 %), K_2O (6 %), Fe_2O_3 (4 %), and MgO (2 %). Its full phase composition, as obtained by the Rietvled full-profile fit to the experimental X-ray diffraction data, is reported in Table 1; further details pertaining to the Rietveld treatment are provided in Fig. S1 and Table S2. Industrial-grade phosphoric acid (75 % H_3PO_4, Chimitex S.p.a.) was diluted with osmotic water to obtain 60 % and 40 % H_3PO_4 solutions. The PGP samples were prepared using 40 %, 60 %, and 75 % H_3PO_4 solutions, keeping a constant activator solution-to-VT mass ratio of 0.9 to isolate the effect of the activator's molarity on the properties of the samples. Exclusively for the samples that underwent leaching tests, phosphoric acid solutions containing stable Cs were prepared by dissolving caesium nitrate ($CsNO_3$, Sigma Aldrich) to simulate radionuclide contamination. The concentration of caesium in the PGP samples was about 300 ppm.

The VT powder was gradually added to the activating solution in a planetary mixer, and the resulting paste was thoroughly homogenised for 5 min. The PGP samples were then cast in cylindrical moulds (diameter 2 cm, height 3 cm) and vibrated to remove air bubbles. The samples not subjected to thermal curing were stored in a climatic chamber at 20 °C (relative humidity >90 %) for 28 days. Those subjected to thermal curing were instead put in a sealed container and kept in an oven at 40 °C or 60 °C for 24 h, then moved to the same climatic chamber for the remaining 27 days. Table 2 summarises the theoretical P/Al, P/Si, and Si/Al molar ratios of the selected PGP formulations and provides a code identifier for each sample.

2.2. Quantitative phase analysis by X-ray diffraction

Powder X-ray diffraction data were collected with an automated

[1] Unless otherwise specified all percentages reported in this work are to be intended as mass percentages.

Table 1
Quantitative phase composition of the investigated VT.

Mineralogical phase	Chabazite	Pyroxene	K-feldspar	Biotite	Ferrierite	Amorphous
Mass fraction (%)	64.7 ± 2	11.7 ± 1	9.5 ± 1	0.5 ± 0.1	0.3 ± 0.1	13.4 ± 1

Table 2
Main theoretical molar ratios of the investigated samples; the activator solution-to-VT ratio of the samples is 0.9 w/w.

	P/Al (mol/mol)	P/Si (mol/mol)	Si/Al (mol/mol)
PGP40-T20, -T40, -T60	1.1	0.42	2.6
PGP60-T20, -T40, -T60	1.6	0.62	2.6
PGP75-T20, -T40, -T60	2.1	0.81	2.6

Nomenclature: PGP*X*-T*Y*, where *X* is the phosphoric acid concentration in % w/w and *Y* is the curing temperature in °C.

Panalytical *X'Pert Pro* modular diffractometer, equipped with a *X'Celerator* detector and under the following operating conditions: 2θ range from 5° to 70° and step size of 0.017°, monochromatized Cu-*K*α radiation, 40 kV, 40 mA, counting time of 240 s per step, top-loaded samples. Phase identification was performed using the *X'Pert HighScore* suite and database. Once all the crystalline components in each sample were identified, quantitative phase analysis was performed by Rietveld full-profile fit to the experimental X-ray diffraction patterns, employing a non-linear least squares procedure and using the GSAS II (*General Structure Analysis System*) software [32]. To perform the Rietveld refinements, the structural models of the identified crystalline phases were imported from the (open) *American Mineralogist Crystal Structure Database* [33]. Through the least squares method, the difference between observed and calculated intensities were minimised, using structural and instrumental parameters as variables, in particular background function (using a Chebeyschev polynomial), crystal size, microstrain, and, in some cases, preferred-orientation correction parameters. For all the samples, convergence was achieved without any significant correlation between the refined parameters, leading to a high quality of fit. To quantify the weight fraction of the amorphous phase, an internal standard was added to the mixture (corundum, 20 %). Further details pertaining to the quantification protocol are provided by *Gualtieri* et al. [34].

2.3. Elemental dissolution tests

To assess aluminium dissolution in the acidic environment, suspensions were prepared with a solid-to-liquid mass ratio of 1:100 of VT in H_3PO_4 solutions with concentrations of 40 %, 60 %, and 75 %. The dissolution of other relevant elements from VT was also investigated, namely iron and silicon. The systems were stirred at 1500 rpm at 20 °C, 40 °C, and 60 °C using a dry bath (Eppendorf ThermoMixer® C). Aliquots were taken after contact times of 20 min, 40 min, 1 h, 2 h, 3 h, and 4 h, and immediately centrifuged at 4000 rpm for 3 min to separate the aqueous phase from the VT powder. The supernatant, after being filtered through a 0.2 μm syringe filter, was then diluted with a 1 % ultrapure nitric acid solution and analysed using an inductively coupled plasma-optical emission spectrometer (ICP-OES, Avio 500, PerkinElmer). Calibration of the spectrometer was performed via matrix-matched certified standard solutions (Inorganic Ventures CMS-x) in the range 1–100 ppm. The released fraction RF_i of the element *i* at time *t* was then calculated as

$$RF_i(t) = m_i(t)/m_{0,i} \tag{1}$$

where $m_i(t)$ is the quantity released from VT and $m_{0,i}$ is its initial content inside the VT, both expressed in terms of mass.

Further insights into the elemental dissolution mechanism in phosphoric acid were obtained by validating the experimental data with theoretical models. As the investigated VT is a multi-phase material, each phase is expected to follow its specific dissolution kinetics. A fully comprehensive model would be the result of the superposition of the dissolution curves of each phase. Since a detailed model is beyond the scope of this work, a simplified approach was adopted, in which the dissolution curves were expressed as the superposition of two pseudo first-order kinetic models according to the following equation:

$$RF_i(t) = C_1{}^*\left(1 - e^{-\lambda_1 t}\right) + C_2{}^*\left(1 - e^{-\lambda_2 t}\right) \tag{2}$$

The first exponential term describes the fast transient associated with the more reactive phase(s), while the second describes the slower transient corresponding to less reactive phase(s). The parameters C_1 and C_2 are the asymptotic released fractions (expressed as weight fractions), while λ_1 and λ_2 are the corresponding dissolution rate coefficients (expressed in h^{-1}).

2.4. Scanning electron microscopy

Morphology characterisation was carried out by scanning electron microscopy (SEM). Samples were analysed by a Zeiss EVO MA10 SEM (Carl Zeiss, Oberkochen Germany). The surfaces of the samples were covered and made conductive by a graphite coating in order to operate in high vacuum mode. The images were acquired at high voltage (20 kV), at room temperature, at different magnifications using both SE and BSE detectors.

2.5. Leaching tests

As requested by the Italian regulator, the semi-dynamic leaching tests were performed for a period of 7 days following the ANSI/ANS-16.1-2019 protocol to evaluate the short-term retention capability of the Cs-loaded PGP samples [35]. As the main objective of this work was to investigate how caesium retention varies based on the PGP phase composition, which is mostly affected by the phosphoric acid concentration, the samples cured at room temperature were selected to be investigated. Osmotic water was used as leachant, and the systems were kept at constant temperature (22 ± 1 °C) for the whole duration of the experiment. The resulting leachates were duly diluted using a 1 % ultrapure HNO_3 solution and subsequently analysed by means of Inductively Coupled Plasma-Mass Spectrometry (ICP-MS, NexION 2000; PerkinElmer) to calculate the contaminant releases. The instrument was calibrated via matrix-matched multi-elemental certified standard solutions (Inorganic Ventures CMS-x) in the range 0.1–100 ppb. The cumulative leached fraction CF_n of caesium up to the *n*-th time interval was calculated as:

$$CF_n = a_n/A_0 \tag{3}$$

where a_n is the leached quantity of caesium up to the *n*-th time interval and A_0 is the total quantity of caesium inside the tested specimen prior to the beginning of the test, both expressed in terms of mass. The leachability index *L* is then calculated according to the ANSI/ANS-16.1-2019 protocol to evaluate the leaching behaviour of the samples and compare it to the Italian WAC [35]. For comparison with existent literature, the leaching rate LR_n of caesium up to the *n*-th time interval was calculated as:

$$LR_n = CF_n{}^*\frac{V}{S}{}^*\frac{1}{t_n} \tag{4}$$

where *V* is the volume of the specimen (in cm^3), *S* its total surface area exposed to water (in cm^2), and t_n is the elapsed time since the beginning

of the test up to the *n*-th time, expressed in days [17].

3. Results and discussion

3.1. Characterisation of the samples

3.1.1. Phase analysis

The results from the QPA-XRD analysis are reported in Table 3. The Rietveld full-profile fit of the QPA-XRD patterns of the PGP samples prepared using 40 %, 60 %, and 75 % H_3PO_4 solutions for the investigated curing temperatures are reported in Figs. 1–3, respectively, while the references of the crystalline structure models used in the Rietveld refinements and the associated statistical parameters are reported in Table S1 and Table S3. All the PGP samples had a largely amorphous component, at least 70 % of the matrix, as expected for GPs [36,37]. This dominant phase is mainly a mixture of non-crystalline alumino-phosphates, silico-phosphates, and alumino-silico-phosphates, constituting the PGP network [38,39]. While QPA-XRD cannot discern the PGP network from other possible amorphous phases, such as amorphous silica, it is nonetheless reasonable to assume that a high degree of reaction occurred in the samples, as the VT was mostly crystalline (about 85 %) before the reaction. Furthermore, pyroxene was completely dissolved in all the samples due to its instability in acidic environments, leading to the release of elements such as Mg, Ca, and Fe [40].

For the PGP40 samples, the total amorphous fraction increases from 70.6 % to 72.9 % and 80.8 % at curing temperatures of 20, 40, and 60 °C, respectively. This might suggest that the initial de-alumination phase of the VT is favoured by the higher temperature, leading to a stronger and more amorphous configuration, as reported in literature [25,26]. In contrast, the amorphous fraction of PGP60 and PGP75 samples was only marginally influenced by the curing temperature, with essentially constant values in the order of 75 % and 83 %, respectively. The higher amorphous content is primarily ascribable to the increase in the activator concentration [27,41]. This suggests that an asymptotic equilibrium is already reached between the phases at 20 °C, thus temperature barely affects the mineralogical composition of the samples.

Chabazite, ideally $(Ca,K_2,Na_2)_2(Al_2Si_4O_{12})_2{\cdot}12H_2O$, the main mineralogical phase of the VT precursor, was heavily dissolved in the PGPs as its aluminosilicate framework breaks down due to lower stability in acidic environments, contrarily to what happens in alkaline conditions [10,42,43]. As reported in Table 3, chabazite was identified only in the three PGP40 samples of lower acidity; approximately 20 % with respect to the initial amount was not dissolved, and the curing temperature did not affect its stability. Increasing the H_3PO_4 solution concentration to at least 60 %, chabazite completely decomposed. The dissolution of chabazite entailed the release of several chemical species in the PGP matrices, such as Ca^{2+} and K^+, that can promote the nucleation and growth of new crystalline phases (as described below), and an amorphous (Al + Si)-rich phase, which contributed to the high non-crystalline fraction detected in the QPA-XRD analysis of the samples prepared using higher acid concentration. As further discussed in section 3.2, the total dissolution of chabazite caused a lower retention capability for Cs in the PGP60 sample, while unexpectedly no significant effects were observed for PGP75.

Taranakite, ideally $K_3Al_5(PO_3OH)_6(PO_4)_2{\cdot}18H_2O$, was the main crystalline phase in the PGP40 and PGP60 samples (Table 3). As reported in literature, its formation is favoured at low pH by precipitation of K^+ with soluble alumino-phosphate complex anions [44,45]. Increasing the concentration of the H_3PO_4 solution from 40 % to 60 % promoted taranakite precipitation, as more K^+ from chabazite dissolution and PO_4^{3-} became available, leading to values in the order of 16 % and 21 %, respectively. Furthermore, this phase exhibited stability under thermal curing except for the PGP40-T60 sample, for which a lower fraction of 8.3 % was measured. A possible explanation for this deviation is that thermal curing at 60 °C promotes the formation of amorphous alumino-(silico-)phosphate phases with superior reactivity. This hypothesis was corroborated by the experimental findings discussed in section 3.1.2, as aluminium dissolution using a 40 % phosphoric acid solution at 60 °C exhibited a significantly faster kinetics than at lower temperatures, thus possibly hindering the formation of crystalline phases.

Calcium as Ca^{2+} can form several phases in PGPs, mostly amorphous calcium-alumino-phosphates and calcium-silico-alumino-phosphates, which favour the precipitation of phases acting as nucleation sites, thus enhancing geopolymerisation kinetics and improving compressive strength [46,47]. In PGP40 and PGP60 samples, calcium-based crystalline phases, due to chabazite dissolution, were not identified, thus it is highly likely that Ca^{2+} is one of the chemical components of the amorphous phase. However, increasing the H_3PO_4 solution concentration to 75 % led to a new dominant calcium dihydrogen phosphate $Ca(H_2PO_4)_2$ crystalline phase, which partially replaced taranakite. The abundance of dihydrogenphosphate anions at low pH, along with and the limited water availability, promoted the formation of this anhydrous acid phosphate over the highly hydrated taranakite. Increasing the curing temperature might instead favour once again the formation of amorphous calcium phosphate phases, coherently with the slight increase in the amorphous fraction of the PGP75 samples. With similar considerations, Mg^{2+} from pyroxene dissolution followed the same chemical behaviour of Ca^{2+} and formed crystalline phases only in the PGP75 samples, while in the other specimens it reasonably formed amorphous magnesium phosphates [48]. Unlike calcium dihydrogen phosphate, bobierrite, ideally $Mg_3(PO_4)_2{\cdot}8H_2O$, was stable regardless of the curing temperature.

Finally, the fraction of K-feldspar, a minor crystalline phase in VT, remained nearly constant among all the samples. K-feldspar exhibited elevated stability against the curing temperature thanks to its strong framework structures [49,50]. Partial dissolution occurred only in the PGP75 samples due to the extremely low initial pH. The use of K-feldspar as PGP precursor was reported to improve durability and mechanical strength, although to a minor extent when compared to alkali GPs due to its limited solubility in phosphoric acid [51,52]. However, due to the reduced fractions contained, this did not result in any significant mineralogical difference across the specimens.

3.1.2. Elemental dissolution tests of VT

Aluminium dissolution from aluminosilicates-rich materials, such as coal fly ash and kaolin, by inorganic acids is known to be effective

Table 3
Quantitative mineralogical phase composition of the PGP samples varying activator concentration and thermal curing; all the values are expressed as mass percentages.

	PGP40			PGP60			PGP75		
	T20	T40	T60	T20	T40	T60	T20	T40	T60
Amorphous	71 ± 2	73 ± 2	81 ± 1	74 ± 2	75 ± 2	75 ± 1	83 ± 3	84 ± 2	85 ± 1
Taranakite $K_3Al_5(PO_3OH)_6(PO_4)_2 \cdot 18H_2O$	17 ± 1	16 ± 1	8.3 ± 0.2	21.6 ± 0.9	21 ± 2	20.5 ± 0.5	4.2 ± 0.3	4.0 ± 0.3	5.4 ± 0.3
K-Feldspar $KAlSi_3O_8$	4.2 ± 0.3	4.0 ± 0.3	3.5 ± 0.1	4.2 ± 0.2	3.8 ± 0.2	4.4 ± 0.1	1.6 ± 0.2	2.1 ± 0.2	2.5 ± 0.2
Chabazite $(Ca,K_2,Na_2)_2(Al_2Si_4O_{12})_2 \cdot 12H_2O$	7.4 ± 0.4	7.2 ± 0.4	7.3 ± 0.1	/	/	/	/	/	/
Calcite $CaCO_3$	0.1 ± 0.1	/	0.1 ± 0.1	/	/	/	0.2 ± 0.1	0.2 ± 0.1	/
Calcium Dihydrogen Phosphate $Ca(H_2PO_4)_2$	/	/	/	/	/	/	9.5 ± 0.4	8.4 ± 0.4	5.3 ± 0.2
Bobierrite $Mg_3(PO_4)_2 \cdot 8H_2O$	/	/	/	/	/	/	1.5 ± 0.2	1.5 ± 0.2	1.6 ± 0.1

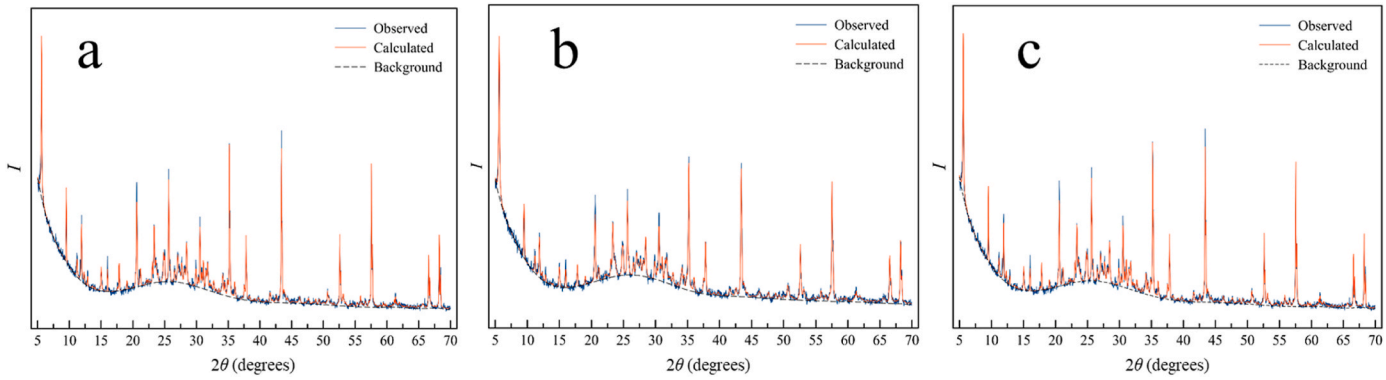

Fig. 1. X-ray diffraction patterns of PGP samples using phosphoric acid 40 % w/w at different thermal curing temperatures: a) 20 °C (PGP40-T20); b) 40 °C (PGP40-T40); c) 60 °C (PGP40-T60).

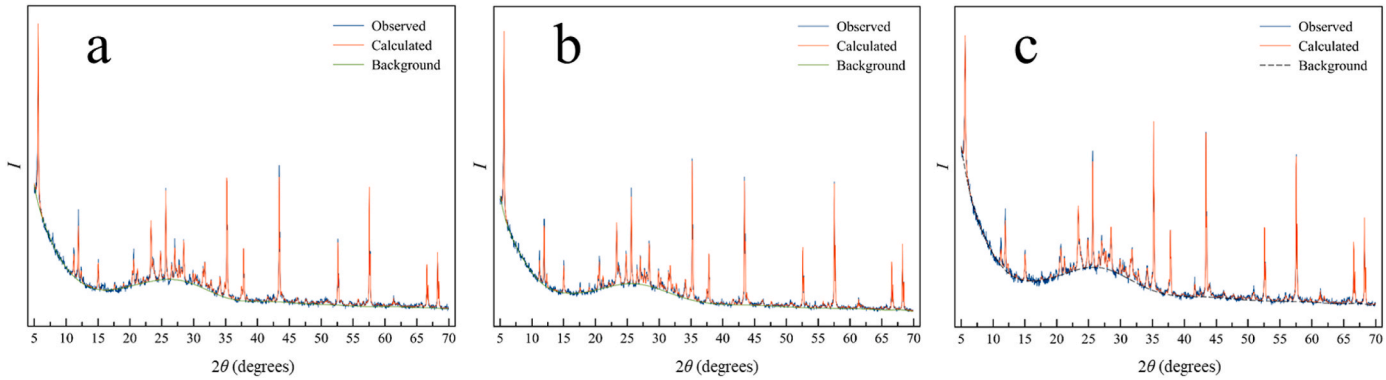

Fig. 2. X-ray diffraction patterns of PGP samples using phosphoric acid 60 % w/w at different thermal curing temperatures: a) 20 °C (PGP60-T20); b) 40 °C (PGP60-T40); c) 60 °C (PGP60-T60).

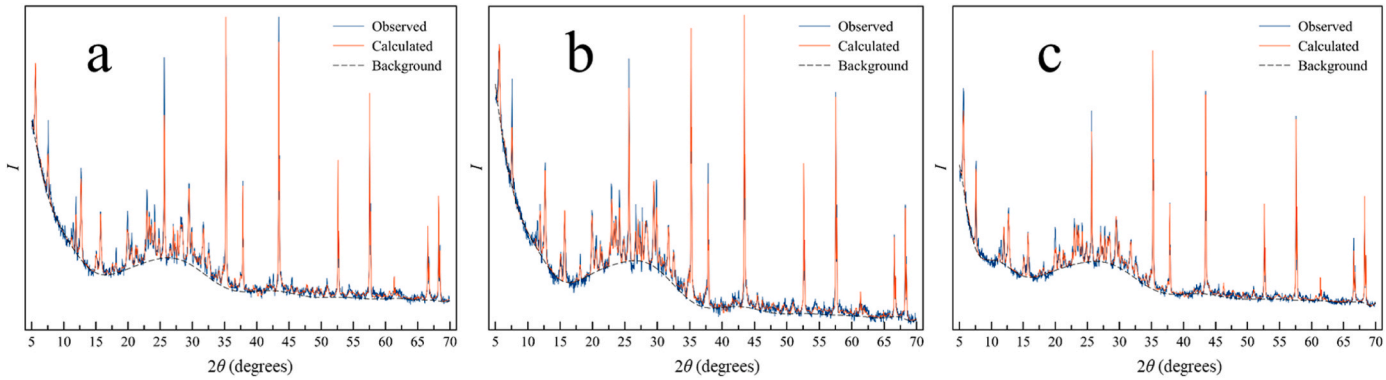

Fig. 3. X-ray diffraction patterns of PGP samples using phosphoric acid 75 % w/w at different thermal curing temperatures: a) 20 °C (PGP75-T20); b) 40 °C (PGP75-T40); c) 60 °C (PGP75-T60).

[53–55]. The main mechanism is the protonation of the bridging oxygens between Al/Si-polyhedra, which significantly lowers the barrier energy of the dissolution reaction [39,56,57]. The dissolution of aluminium from VT over the time, at the investigated phosphoric acid concentrations and temperatures, is shown in Fig. 4. Increasing the phosphoric acid concentration beyond 40 % leads to a reduction in the total amount of aluminium released over 4 h and slower kinetics. This is likely because the viscosity of phosphoric acid solutions strongly increases with the concentration, hence limiting diffusion and hindering aluminium dissolution [58,59]. Comparing the curves after 4 h at 20 °C, the aluminium release decreased from approximately 51 %–32 % and 9 % for phosphoric acid concentrations equal to 40 %, 60 %, and 75 %, respectively. Increasing the temperature promoted aluminium dissolution and accelerated the kinetics of this process [60]; this is coherent with the increase in reaction kinetics and the decrease in solution viscosity, which are typically proportional to the temperature. In fact, after 4 h at 60 °C, the aluminium release amounted to approximately 66 %, 63 %, and 34 %, for phosphoric acid concentrations of 40 %, 60 %, and 75 %, respectively.

All the dissolution curves were well described by the model proposed in equation (2). The optimal model parameters and the corresponding coefficients of determination R^2 are reported in Table 4. Given the time resolution of the experimental data points, it was not feasible to directly and accurately determine the values of λ_1, and it can only be inferred

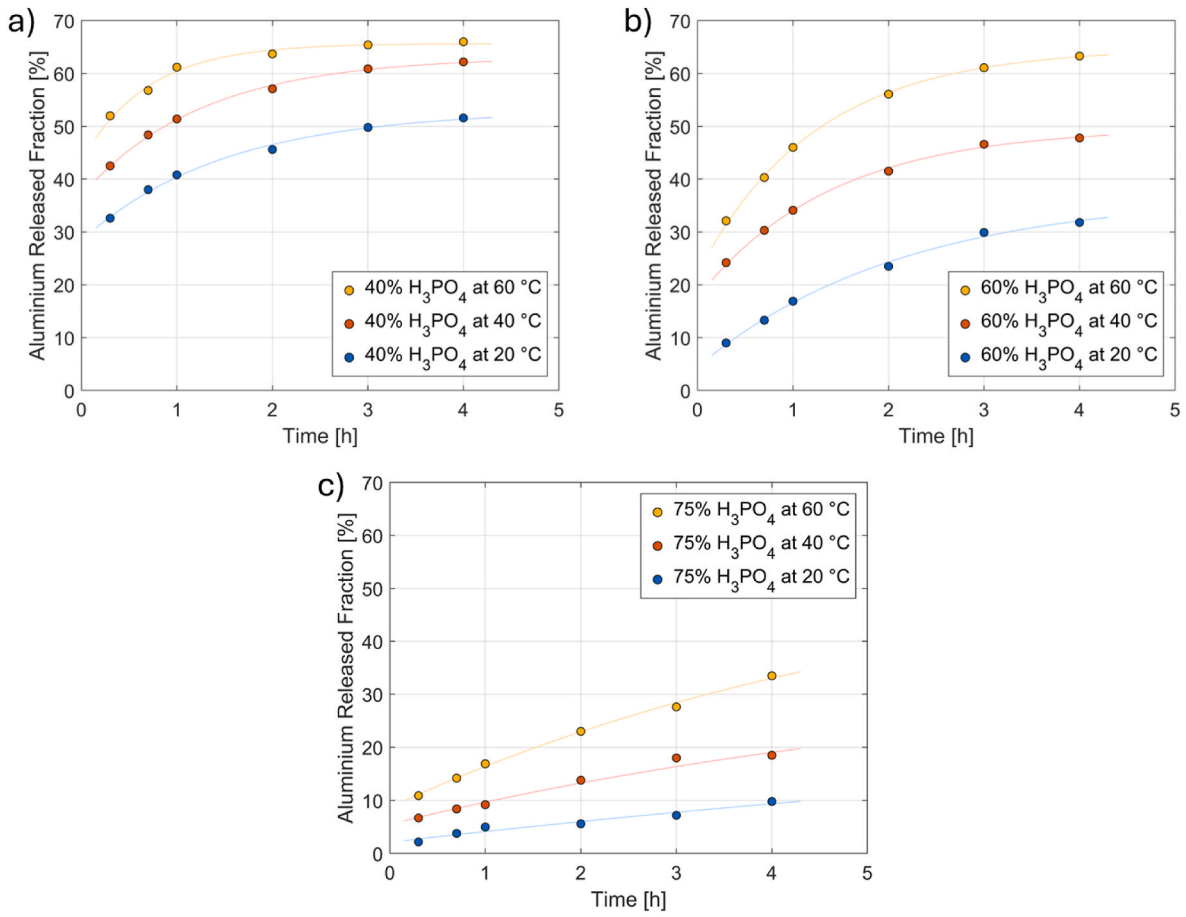

Fig. 4. Dissolution curves of aluminium at 20, 40, and 60 °C in phosphoric acid solutions of different concentrations: a) 40 % b) 60 % c) 75 % w/w; error bars are within markers size. The interpolation represents only the slower transient of the overall dissolution curve.

Table 4
Model parameters for the dissolution curves of aluminium and iron.

		Aluminium				Iron			
	T [°C]	C_1	λ_2 [h^{-1}]	C_2	R^2	C_1	λ_2 [h^{-1}]	C_2	R^2
40 %	20	0.28	0.66	0.25	0.992	0.11	0.56	0.25	0.924
	40	0.37	0.79	0.26	0.996	0.21	0.65	0.36	0.997
	60	0.43	1.44	0.22	0.990	0.27	1.23	0.39	0.988
	T [°C]	C_1	λ_2 [h^{-1}]	C_2	R^2	C_1	λ_2 [h^{-1}]	C_2	R^2
60 %	20	0.04	0.47	0.33	0.997	0.11	0.53	0.28	0.990
	40	0.18	0.72	0.32	0.998	0.22	0.69	0.40	0.998
	60	0.22	0.81	0.43	0.998	0.28	2.06	0.38	0.980
	T [°C]	C_1	λ_2 [h^{-1}]	C_2	R^2	C_1	λ_2 [h^{-1}]	C_2	R^2
75 %	20	0.02	0.07	0.28	0.948	0.12	0.61	0.23	0.995
	40	0.06	0.15	0.30	0.972	0.21	0.73	0.37	0.998
	60	0.09	0.17	0.49	0.996	0.41	1.59	0.22	0.981

that the first exponential contribution to the kinetic model reaches its equilibrium well before 20 min contact time. For this reason, λ_1 values are not reported and only the asymptotic released fractions C_1 were inferred and reported in Table 4. Consistently with what was previously described, most of the aluminium release occurred within the first 20 min when using a 40 % phosphoric acid solution, between roughly 30 % and 50 % depending on the temperature. This high reactivity can be linked to chabazite and pyroxene instability in acidic media, which favours their rapid dissolution. Furthermore, it is worth highlighting that, with a 60 % phosphoric acid solution, the effect of temperature was noticeably beneficial, as the values of C_1 increased by a factor of about 5 at 40 °C and 60 °C. Once again, this finding highlights the advantages of adopting a thermal curing to improve sample setting, in particular when increasing the activator concentration. In fact, a higher content of readily available aluminium in the PGP paste results in a shorter duration of the de-alumination phase, which is recognised to be the most important factor influencing the setting time of these binders [21,26,39]. Finally, summing the terms C_1 and C_2 it was possible to estimate the total asymptotic aluminium release from the VT. When using either a 40 % or 60 % phosphoric acid solution, the resulting values were closely matched with the released fraction after 4 h, meaning that the dissolution reaction is almost completed by that time. Furthermore, in three out

of these six tests, a steady-state aluminium release of approximately 65 % was measured (Fig. 4), suggesting that this might represent the maximum achievable value under the investigated experimental conditions. Conversely, when using a 75 % phosphoric acid solution, the sum of C_1 and C_2 was higher than the experimental value after 4 h by a factor of about 2–3 based on the temperature, confirming that an excessive activator concentration slows down the de-alumination process.

Further insights into the effects of the phosphoric acid concentration and temperature can be inferred from the dissolution rate coefficient λ_2, which expressed sensitivity to the experimental parameters. The value of λ_2 increased by 20 % and 119 % when the temperature was raised from 20 °C to 40 °C and 60 °C, respectively, using a 40 % phosphoric acid solution (Table 4). The significant acceleration of the reaction kinetics at 60 °C, leading to the dissolution of about half of the aluminium from the VT precursor already within the first 20 min, is coherent with the reduced content of taranakite in the PGP40-T60 sample, as reported in section 3.1.1. Under these conditions, in fact, the de-alumination reaction might be so fast that crystal formation is hindered in favour of amorphous phase development. Similarly, for 60 % phosphoric acid the value of λ_2 increased by 54 % at 40 °C and 73 % at 60 °C. However, even the latter value remained significantly lower than that observed for the 40 % phosphoric acid at 60 °C, which may account for the fact that crystalline taranakite formation was not hindered. In contrast, the values of λ_2 in the aluminium dissolution tests with 75 % phosphoric acid were one order of magnitude lower, although the beneficial effects of increasing the temperature were again confirmed.

Iron is an element of particular importance in PGPs, as it can partially replace aluminium to form ferro-sialate structures (−O−Fe−O−Si−O−Al−O−) or amorphous iron phosphate phases [61]. As these reactions are strongly exothermic, the generated heat accelerates the formation of the PGP binder, hence reducing the setting time, and improves mechanical properties by fostering a denser matrix [62, 63]. The dissolution of iron over time at the investigated phosphoric acid concentrations and temperatures is shown in Fig. 5. All the nine investigated combinations of phosphoric acid concentration and temperature followed the model from equation (2); the corresponding parameters are reported in Table 4. The releases were considerably high as iron is easily leached in phosphoric acid solutions [64]. Contrarily to literature data, the phosphoric acid concentration had no significant effect on the total quantity of iron dissolved from the VT [64]. Instead, as expected, temperature was the main factor influencing iron dissolution [65], both in terms of kinetics and of total released amount. After 4 h contact time at 20 °C, iron release in the 40 % phosphoric acid solution was about 32 %, and it increased to 54 % at 40 °C and 66 % at 60 °C. Comparable values were also measured for the other two phosphoric acid solutions. Temperature was confirmed to be the main factor influencing the kinetics, in particular regarding early-stage dissolution. Specifically, the parameter C_1 increased approximately by a factor 2 rising the temperature to 40 °C, and about 3–60 °C, regardless the phosphoric acid concentration. Moreover, the total asymptotic iron dissolution, estimated as the sum of the terms C_1 and C_2, also showed no dependence on the phosphoric acid solution. The corresponding values were around 36 % at 20 °C, 59 % at 40 °C, and 65 % at 60 °C, comparable to the released fraction after 4 h, hence the dissolution reaction is almost completed within 4 h.

Silicon releases were very limited when compared to aluminium and iron, as the majority of silicon compounds, in particular silica, are chemically inert in most acids other than hydrofluoric acid [66].

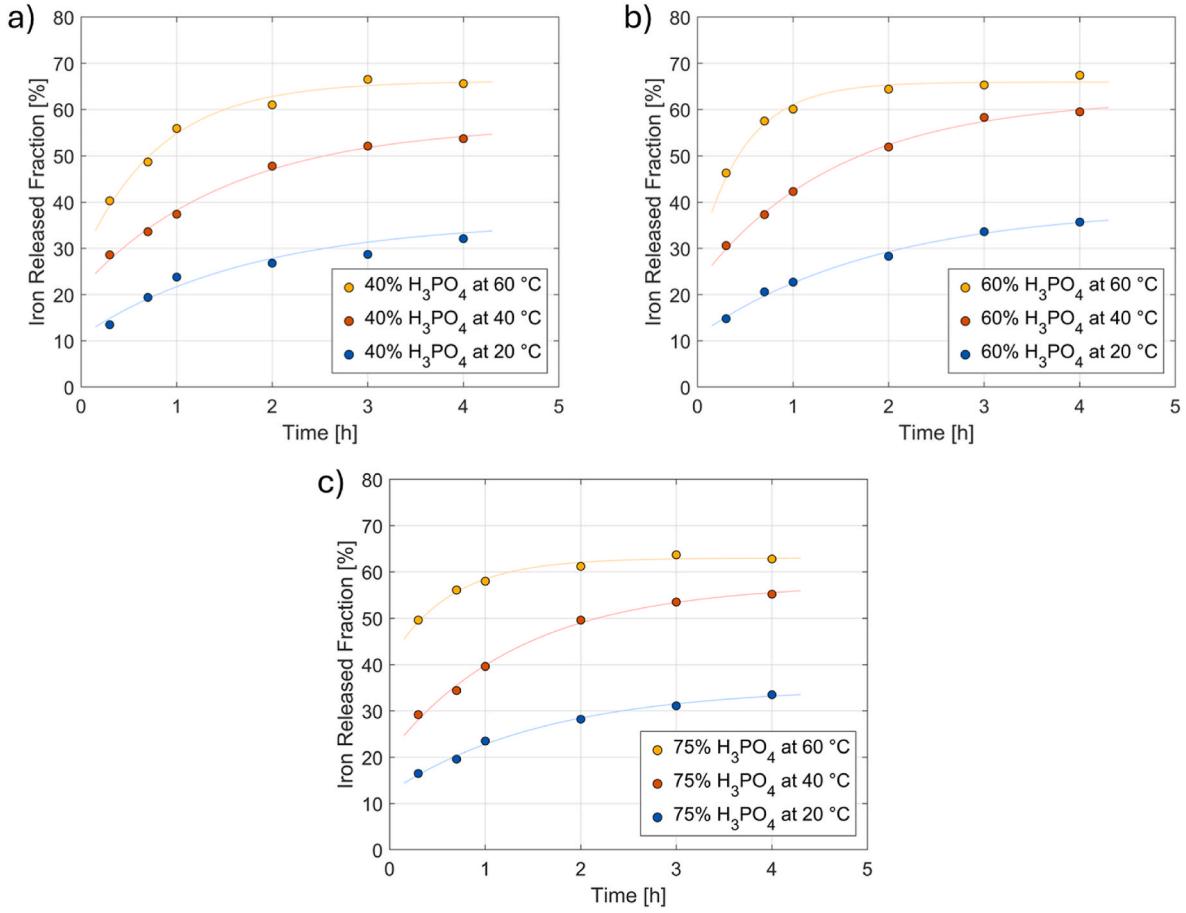

Fig. 5. Dissolution curves of iron at 20, 40, and 60 °C in phosphoric acid solutions of different concentrations: a) 40 % b) 60 % c) 75 % w/w; error bars are within markers size. The interpolation represents only the slower transient of the overall dissolution curve.

According to *Bu* et al., phosphoric acid exhibits greater silicon dissolution from aluminosilicate precursors than aluminium dihydrogen phosphate, another common PGP activator [56]. However, its effectiveness remains limited as phosphoric acid can dissolve silicon only through protonation of oxygen in the siloxo (−Si−O−Si−) bonds, which are more resistant to protonation than sialate (−Al−O−Si−) bonds [39,56]. In opposition to aluminium and iron, no clear silicon dissolution trends were observed. Expectedly, temperature had no significant effect on dissolution, as silicon compounds commonly found in geopolymers are stable at the investigated temperatures range [67]. After 4 h of contact, the silicon releases in the 40 % and 60 % phosphoric acid solutions were considerably low, in the order of 1 % and 2 % respectively, as already observed in other literature works on PGPs [25,68]. Instead, silicon releases increased to about 6 % when using 75 % phosphoric acid solutions. This higher dissolution rate can reflect the higher acid concentration and, to some extent, even the partial consumption of K-feldspar at very low pH, as consistently reported in section 3.1.1 for the PGP75 samples. As expected, all the results were considerably lower than those reported in literature using alkaline solutions [69,70]. It is important to highlight that as silicon is only marginally dissolved in phosphoric acid, only a small fraction is able to actively participate in the formation of the geopolymeric gel. Consequently, the effective P/Si ratio of the PGP binder is expectedly higher than the theoretical total P/Si ratio. Without accurate estimations, the optimisation of PGP formulations might be based on misleading data, potentially compromising the quality of the final specimens [69].

3.1.3. *Morphology of the samples*

The micrographs of a selection of PGP samples are shown in Figs. 6 and 7. All the samples showed a typical texture ascribable to polyphasic aggregates, with a dominant amorphous phase, consistently with the experimental findings based on QPA-XRD results.

The effects of thermal curing on the morphology of the samples were noticeable mostly on the PGP40 samples, as shown in Fig. 6. Although chabazite was detected by QPA-XRD, it was not possible to clearly identify its crystals, being a microcrystalline phase that heavily reacted within the system, thus resulting covered by the geopolymeric network. This can be inferred from the PGP40-T20 sample, shown in Fig. 6a. The PGP40-T60 sample presented relatively diffused microcracks (Fig. 6b), attributable to shrinkage due to the high water content and the relatively elevated curing temperature, both of which might favour sample exsiccation [25,71]. Therefore, although increasing the curing temperature to 60 °C led to a more abundant and compact amorphous gel, promoted by the higher degree of polymerisation, the overall mechanical performance and Cs retention capability of the sample might be hindered by the microcracks.

The evolution of the crystalline phases was mostly appreciable on the PGP samples that underwent thermal curing at 60 °C (Fig. 7). Considering the low fraction of taranakite and the difficulty to detect pure chabazite phases, the PGP40-T60 sample showed a vastly amorphous microstructure (Fig. 7a). In the PGP60-T60 sample, instead, taranakite

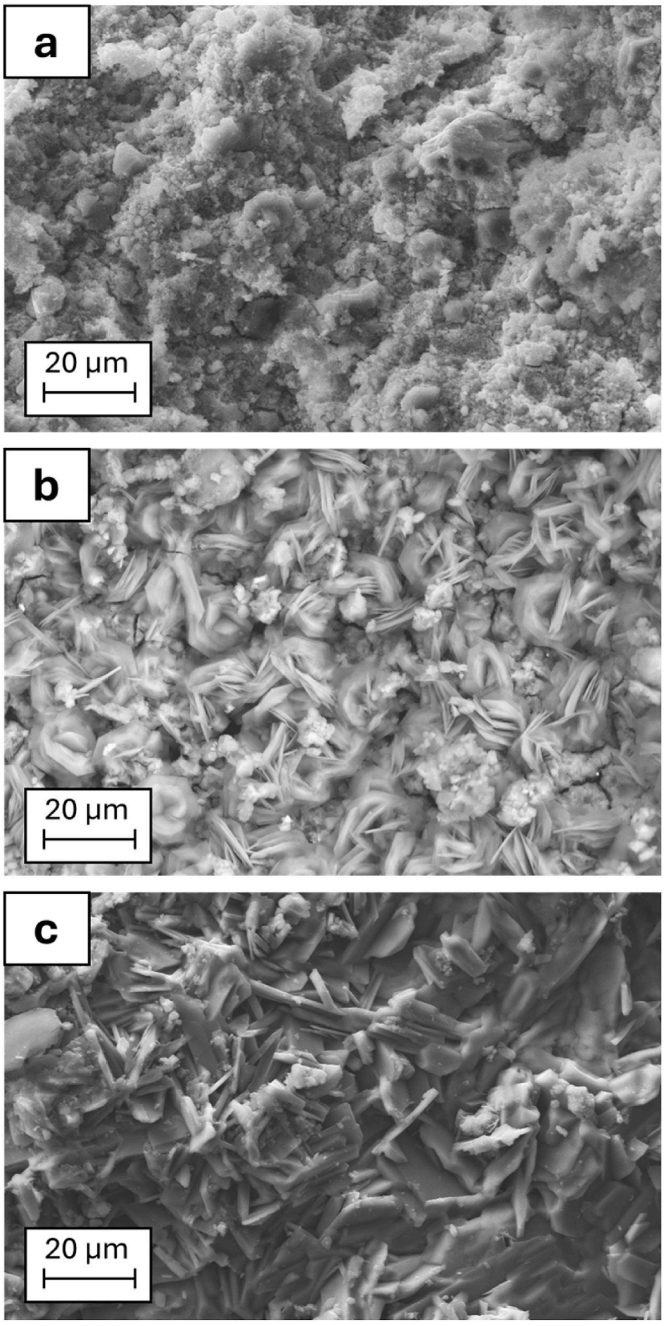

Fig. 7. SEM micrographs (2000 × magnification) of PGP samples at different phosphoric acid concentrations that underwent thermal curing at 60 °C: a) 40 % w/w (PGP40-T60); b) 60 % w/w (PGP60-T60); c) 75 % w/w (PGP75-T60).

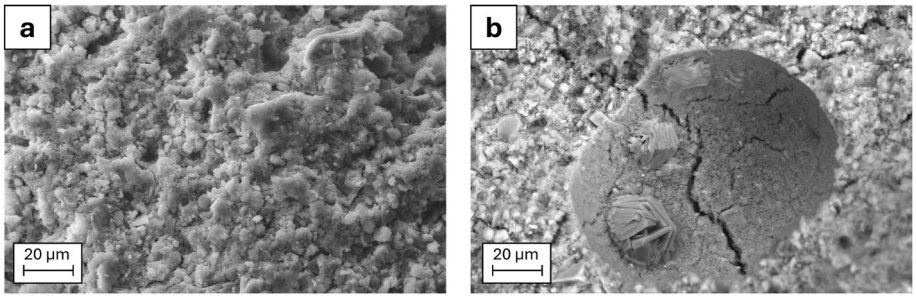

Fig. 6. SEM micrographs (2000 × magnification) of PGP samples using phosphoric acid 40 % w/w at different thermal curing temperatures: a) 20 °C (PGP40-T20); b) 60 °C (PGP40-T60).

crystals were more easily recognisable and homogeneously dispersed throughout the matrix (Fig. 7b), with a lamellar habit with interpenetrated individuals. In the PGP75 samples, as previously reported in section 3.1.1, taranakite formation was competitive to the formation of calcium dihydrogenphosphate (Table 3). Consistently, this phase was identified in the PGP75-T60 sample (Fig. 7c). In opposition to taranakite, calcium dihydrogen phosphate formed platy crystals that were more localised into clusters.

3.2. Leaching behaviour

Compared to ordinary Portland cement, alkaline GPs typically exhibit superior Cs^+ retention capabilities [72]. Conversely, thanks to their positive surface charge, PGPs are typically more effective for the stabilisation of wastes containing anionic species, such as Se and I oxyanions and I^- [15]. Although PGPs are less suited for cation retention for this same reason, it is possible to improve their immobilisation performances by opportunely tuning the P/Al ratio, thus modifying the surface charge up to slightly positive or neutral values [18]. Caesium retention in PGPs is typically lower than in alkaline GPs, but they are sufficiently well performing to meet the WAC established by regulatory bodies [17].

The leaching behaviour of caesium-loaded PGP40-T20, PGP60-T20, and PGP75-T20 samples was investigated. The cumulative leached fractions of Cs^+ from the matrices, shown in Fig. 8a, followed a linear trend with respect to the square root of time, implying that the predominant leaching mechanism was diffusion [11]. After 7 days, the PGP40-T20 sample released only 1.7 % by weight of the initially loaded caesium. This low fraction can be attributed to the partial preservation of chabazite from the VT, which contributed to the improvement of the leaching resistance. Instead, PGP60-T20 exhibited a worse retention capability. As previously discussed in section 3.1.1, the total consumption of chabazite might hinder caesium immobilisation. Moreover, an increase in the P/Al corresponds to a more positively charged surface, thus a higher repulsion for cations [15]. Nevertheless, the 7-day cumulative leached fraction still remained considerably low at approximately 3.3 % by weight, suggesting the involvement of other retention mechanisms counterbalancing the adverse effects from electrostatic repulsion and chabazite consumption. As taranakite is an abundant phase in the PGP40 and PGP60 samples, it is possible for Cs^+ to form taranakite-like crystals substituting to K^+ due to their similar chemical behaviour. Since taranakite is relatively insoluble in water, caesium leaching is likely hindered [73]. Unexpectedly, the PGP75-T20 sample exhibited comparable results to the PGP40-T20 sample, despite the absence of chabazite and a much higher P/Al ratio, i.e. a stronger cation electrostatic repulsion. A possible explanation for this phenomenon is that the formation of new phases was favoured by the abundance of phosphate and dihydrogen phosphate anions, such as highly insoluble magnesium caesium phosphates [74]. Furthermore, the higher amorphous fraction of the PGP75-T20 sample may have contributed to a more compact microstructure of the material, enhancing physical retention of caesium and limiting its diffusion [17].

The leaching rates of Cs^+, shown in Fig. 8b, decreased over time after an initial surface wash-off [17,75]. Consistently with the previously discussed results, the leaching rates for the PGP40-T20 and PGP75-T20 samples were comparable, ranging from about $1.3{\cdot}10^{-3}$ cm/d after one day to $0.8{\cdot}10^{-3}$ cm/d after seven days. Instead, the values for the PGP60-T20 sample were higher by a factor roughly two, namely $2.3{\cdot}10^{-3}$ cm/d and $1.6{\cdot}10^{-3}$ cm/d after one and seven days, respectively. Nonetheless, all values remained considerably low in absolute terms.

As required by the Italian national regulator, the leachability index for Cs^+ was calculated over a 7-day test to quantitatively estimate the retention capability of the samples [76]. The leachability index value for both the PGP40-T20 and PGP75-T20 samples was 10.2 ± 0.1, while for the PGP60-T20 sample it was slightly lower, namely 9.6 ± 0.1. Nevertheless, all values were significantly above the minimum threshold of 6.0 required by the Italian WAC [76].

Finally, a comparison between caesium retention capabilities of ordinary Portland cement, alkali GP, and PGPs from the literature is reported in Table 5. Although PGP40-T20 and PGP75-T20 demonstrated almost identical retention capabilities, the first one was chosen as the reference sample for this study. This choice was made due to the lower concentration of the activator, which allows to reduce costs and have a more workable paste due to its lower viscosity. When compared to ordinary Portland cement, PGP40-T20 demonstrated a one order of magnitude lower cumulative Cs^+ leached fraction, and one to two orders of magnitude lower leaching rate after 7 days. The comparison with alkali GPs was instead more variable, as some alkali GPs outperformed PGPs, while others showed similar results. This indicates that PGPs represent a promising class of materials for Cs^+ immobilisation, especially for acidic wastes difficult to incorporate within alkaline matrices without pre-treatments. To the best of the authors' knowledge, all relevant studies addressing Cs^+ leaching from PGPs are reported in Table 5. Although the results presented in this study are particularly promising in comparison to prior literature, further research is necessary to corroborate these findings and to better investigate caesium retention mechanisms, especially on a long-term horizon.

4. Conclusions

In this study, PGPs were prepared using a natural chabazite-rich VT

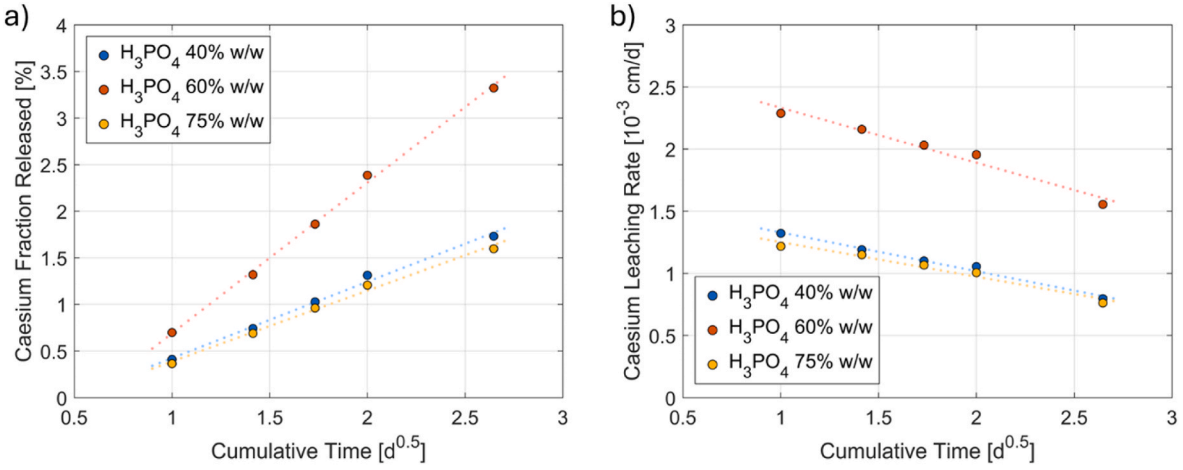

Fig. 8. Caesium a) cumulative leached fraction and b) leaching rate in the investigated PGP samples; error bars are within markers size.

Table 5
Comparison between the leaching performance of the PGP40-T20 sample and other cementitious matrices.

Type of matrix	Cs release after 7 days	Cs leaching rate after 7 days [10^{-3} cm/d]	Cs Leachability Index	Ref
This study's PGP40-T20	1.7 %	0.8	10.2	/
OPC	~20 %	~6.5	/	[29] *
OPC	~45 %	~30	7.0	[77] *
Alkali GP with fly ash	~2 %	~1.4	10.2	[77] *
Alkali GP with metakaolin	~1.5 %	~0.5	/	[29] *
Alkali GP with various precursors, loaded with treated ion exchange resins	~0.1 %	~0.04	11.2	[11] *
PGP with metakaolin	~3 %	~1.4	/	[18] *
PGP with metakaolin, loaded with spent ion exchange resins	~7 %	~20	8.9	[17]

Nomenclature: OPC, Ordinary Portland Cement; GP, Geopolymer; PGP, Phosphate-based Geopolymer. * Data were adapted for comparison purposes.

as precursor to evaluate their suitability for radioactive waste conditioning. The influence of the phosphoric acid concentration and curing temperature on the phase evolution was systematically investigated. The key findings are hereby summarised.

- Chabazite was found to be highly unstable in acidic environments. The QPA-XRD analysis revealed that chabazite remained in small weight fraction when using a 40 % phosphoric acid solution as activator, and it was fully dissolved using 60 % and 75 % phosphoric acid solutions. Such a dissolution resulted, during the first steps of geopolymerisation, in the release of high amounts of structural aluminium, in addition to potassium and calcium as chabazite balancing cations.
- The VT dissolution tests confirmed that increasing temperature promotes aluminium release. Readily available aluminium plays a key role in reducing the duration of the de-alumination phase, which controls the setting time of these binders. In contrast, silicon release was more limited and mostly influenced by phosphoric acid concentration, with no significant temperature dependence.
- All the selected formulations exhibited promising short-term caesium retention capabilities (retention of approximately 98 % after 7 days), significantly outperforming ordinary Portland cement-based matrices, and matching the performances of some alkali-activated geopolymers. Furthermore, the selected formulations met the Italian leaching WAC for low-to-intermediate level radioactive waste disposal.

Chabazite-rich VT thus emerges as a particularly promising precursor for PGP formulations. Furthermore, its elevated resistance to Cs leaching makes it a promising precursor for applications within radioactive waste conditioning. Given that the effects of thermal curing on PGPs have only recently been explored, and primarily for a limited selection of precursors, the outcomes of this paper provided a meaningful contribution to the literature.

Future works will focus on fully elucidating the mechanisms behind caesium immobilisation in these samples. Furthermore, the leaching of other common radionuclides will be investigated, focusing on both cationic (e.g., Sr^{2+}, Co^{2+}) and anionic (e.g., I^-, IO_3^-, SeO_4^{2-}, MoO_4^{2-}, Cl^-) species.

CRediT authorship contribution statement

Fabio Fattori: Writing – original draft, Visualization, Validation, Methodology, Investigation, Data curation, Conceptualization. **Gabriele Magugliani:** Writing – review & editing, Validation, Supervision, Methodology. **Giuseppe Marinelli:** Writing – review & editing, Methodology. **Davide Comboni:** Writing – review & editing, Investigation, Data curation. **Giacomo Diego Gatta:** Writing – review & editing, Investigation, Data curation. **Alessandro Girella:** Writing – review & editing, Investigation. **Chiara Milanese:** Writing – review & editing, Investigation, Data curation. **Andrea Santi:** Writing – review & editing, Visualization, Validation. **Francesco Galluccio:** Writing – review & editing, Validation. **Ilaria Moschetti:** Writing – review & editing, Visualization. **Simona Šandalová:** Writing – review & editing. **Elena Macerata:** Writing – review & editing. **Mario Mariani:** Resources, Funding acquisition. **Eros Mossini:** Writing – review & editing, Supervision, Project administration, Funding acquisition, Conceptualization.

Declaration of competing interest

The authors declare that they have no known competing financial interests or personal relationships that could have appeared to influence the work reported in this paper.

Acknowledgements

This work was conducted within the EURAD-2 project. EURAD-2 is co-funded by the European Union under Grant Agreement n° 101166718. The authors thank Fertenia S.r.l. (Italy) for the provided volcanic tuff (Zeolite Fertenia™).

Appendix A. Supplementary data

Supplementary data to this article can be found online at https://doi.org/10.1016/j.ceramint.2025.11.131.

References

[1] K. Goryunova, Y. Gahramanli, V. Muradkhanli, P. Nadirov, Phosphate-activated geopolymers: advantages and application, RSC Adv. 13 (43) (2023) 30329–30345, https://doi.org/10.1039/D3RA05131E.
[2] Y.-S. Wang, Y. Alrefaei, J.-G. Dai, Silico-aluminophosphate and alkali-aluminosilicate geopolymers: a comparative review, Front. Mater. 6 (May 2019), https://doi.org/10.3389/fmats.2019.00106.
[3] Tan Dollente, Promentilla, Life cycle assessment of precast geopolymer products, Chem Eng Trans (Oct. 2021).
[4] J.I.T. Garces, I.J. Dollente, A.B. Beltran, R.R. Tan, M.A.B. Promentilla, Life cycle assessment of self-healing geopolymer concrete, Clean Eng Technol 4 (Oct. 2021) 100147, https://doi.org/10.1016/j.clet.2021.100147.
[5] M. Nodehi, V.M. Taghvaee, Alkali-activated materials and geopolymer: a review of common precursors and activators addressing circular economy, Circ. Econ. Sustain. 2 (1) (Mar. 2022) 165–196, https://doi.org/10.1007/s43615-021-00029-w.
[6] A. Nikolov, I. Rostovsky, H. Nugteren, Geopolymer materials based on natural zeolite, Case Stud. Constr. Mater. 6 (Jun. 2017) 198–205, https://doi.org/10.1016/j.cscm.2017.03.001.
[7] K. Tan, X. Cai, K. Tan, K.Y. Kwan, A review of natural and anthropogenic radionuclide pollution in marine bivalves, Sci. Total Environ. 896 (Oct. 2023) 165030, https://doi.org/10.1016/j.scitotenv.2023.165030.
[8] M.I. Balonov, Internal Exposure of Populations to Long-Lived Radionuclides Released into the Environment, 2007, pp. 120–140, https://doi.org/10.1002/9780470515006.ch9.
[9] E. Mossini, et al., Pre-impregnation approach to encapsulate radioactive liquid organic waste in geopolymer, J. Nucl. Mater. 585 (Nov. 2023) 154608, https://doi.org/10.1016/j.jnucmat.2023.154608.
[10] A. Santi, et al., Design of sustainable geopolymeric matrices for encapsulation of treated radioactive solid organic waste, Front. Mater. 9 (Oct. 2022), https://doi.org/10.3389/fmats.2022.1005864.
[11] F. Galluccio, et al., Pre-disposal management of spent ion-exchange resins by Fenton oxidation treatment and conditioning in an alkali-activated matrix, Nucl. Eng. Des. 429 (Dec. 2024) 113621, https://doi.org/10.1016/j.nucengdes.2024.113621.
[12] M. Arbel-Haddad, Y. Harnik, Y. Schlosser, A. Goldbourt, Cesium immobilization in metakaolin-based geopolymers elucidated by 133Cs solid state NMR spectroscopy,

J. Nucl. Mater. 562 (Apr. 2022) 153570, https://doi.org/10.1016/j.jnucmat.2022.153570.
[13] Z. Chen, et al., Cold reaction sintering of geopolymers for enhanced Cs+ immobilization: synthesis, characterization, and leaching behavior, J. Eur. Ceram. Soc. 45 (6) (Jun. 2025) 117166, https://doi.org/10.1016/j.jeurceramsoc.2024.117166.
[14] R. Sharma, K.K. Das, S. Siddique, J.G. Jang, Cesium immobilization of high pH and low pH belite-rich cement under varying temperature, J Hazard Mater 469 (May 2024) 133995, https://doi.org/10.1016/j.jhazmat.2024.133995.
[15] X. Niu, Y. Elakneswaran, N. Hiroyoshi, Surface chemistry and radionuclide anion immobilisation potential of phosphoric acid-activated metakaolin-based geopolymers, Cem Concr Res 181 (Jul. 2024) 107549, https://doi.org/10.1016/j.cemconres.2024.107549.
[16] X. Niu, Y. Elakneswaran, C.R. Islam, J.L. Provis, T. Sato, Adsorption behaviour of simulant radionuclide cations and anions in metakaolin-based geopolymer, J Hazard Mater 429 (May 2022) 128373, https://doi.org/10.1016/j.jhazmat.2022.128373.
[17] B. Kim, et al., Assessment of structural stability and leaching characteristics of phosphate-based geopolymer waste form containing radioactive spent ion exchange resins, J. Nucl. Mater. 607 (Mar. 2025) 155671, https://doi.org/10.1016/j.jnucmat.2025.155671.
[18] G. Tan, et al., Phosphoric acid-activated metakaolin-based geopolymer: optimizing P/A molar ratio to solidify Cs+ and Sr2+ in nuclear waste, Nucl. Eng. Des. 424 (Aug. 2024) 113300, https://doi.org/10.1016/j.nucengdes.2024.113300.
[19] J.R. Njimou, et al., Removal of lead ions from aqueous solution using phosphate-based geopolymer cement composite, Journal of Chemical Technology & Biotechnology 96 (5) (May 2021) 1358–1369, https://doi.org/10.1002/jctb.6657.
[20] H. Zeng, et al., Comparative study on the preparation of phosphate-based geopolymers using different activators, Constr. Build. Mater. 437 (Jul. 2024) 137000, https://doi.org/10.1016/j.conbuildmat.2024.137000.
[21] Y.-S. Wang, J.L. Provis, J.-G. Dai, Role of soluble aluminum species in the activating solution for synthesis of silico-aluminophosphate geopolymers, Cem. Concr. Compos. 93 (Oct. 2018) 186–195, https://doi.org/10.1016/j.cemconcomp.2018.07.011.
[22] S. Shakib, M.N. Sheikh, M.N.S. Hadi, Effect of the viscosity of alkali activators on the particle packing of geopolymer mortar, J. Mater. Civ. Eng. 37 (3) (Mar. 2025), https://doi.org/10.1061/JMCEE7.MTENG-18711.
[23] L. Gao, Y. Zheng, Y. Tang, J. Yu, X. Yu, B. Liu, Effect of phosphoric acid content on the microstructure and compressive strength of phosphoric acid-based metakaolin geopolymers, Heliyon 6 (4) (Apr. 2020) e03853, https://doi.org/10.1016/j.heliyon.2020.e03853.
[24] M. He, Z. Yang, N. Li, X. Zhu, B. Fu, Z. Ou, Strength, microstructure, CO2 emission and economic analyses of low concentration phosphoric acid-activated fly ash geopolymer, Constr. Build. Mater. 374 (Apr. 2023) 130920, https://doi.org/10.1016/j.conbuildmat.2023.130920.
[25] H. Lin, H. Liu, Y. Li, X. Kong, Properties and reaction mechanism of phosphoric acid activated metakaolin geopolymer at varied curing temperatures, Cem Concr Res 144 (Jun. 2021) 106425, https://doi.org/10.1016/j.cemconres.2021.106425.
[26] J.N.Y. Djobo, Moustapha, L.P.T. Ndjonnou, K.K. Etame, D. Stephan, The role of curing temperature and reactive aluminum species on characteristics of phosphate geopolymer, RSC Adv. 12 (46) (2022) 29653–29665, https://doi.org/10.1039/D2RA04562A.
[27] H.K. Tchakouté, C.H. Rüscher, E. Kamseu, F. Andreola, C. Leonelli, Influence of the molar concentration of phosphoric acid solution on the properties of metakaolin-phosphate-based geopolymer cements, Appl. Clay Sci. 147 (Oct. 2017) 184–194, https://doi.org/10.1016/j.clay.2017.07.036.
[28] H. Baykara, A. Riofrio, M. Cornejo, Preparation, characterization, and environmental impact analysis of natural Ecuadorian zeolite tuff-based silicoaluminophosphate geopolymer, Constr. Build. Mater. 438 (Aug. 2024) 137126, https://doi.org/10.1016/j.conbuildmat.2024.137126.
[29] R.I. Chaerun, et al., Retention mechanism of cesium in chabazite embedded into metakaolin-based alkali activated materials, J Hazard Mater 440 (Oct. 2022) 129732, https://doi.org/10.1016/j.jhazmat.2022.129732.
[30] W. Baek, S. Ha, S. Hong, S. Kim, Y. Kim, Cation exchange of cesium and cation selectivity of natural zeolites: chabazite, stilbite, and heulandite, Microporous Mesoporous Mater. 264 (Jul. 2018) 159–166, https://doi.org/10.1016/j.micromeso.2018.01.025.
[31] F. Galluccio, et al., iRE-SOLVE process for the pre-disposal management of spent ion-exchange resins, Ind. Eng. Chem. Res. 64 (20) (May 2025) 10347–10351, https://doi.org/10.1021/acs.iecr.5c01196.
[32] B.H. Toby, R.B. Von Dreele, GSAS-II : the genesis of a modern open-source all purpose crystallography software package, J. Appl. Crystallogr. 46 (2) (Apr. 2013) 544–549, https://doi.org/10.1107/S0021889813003531.
[33] R.T. Downs, M. Hall-Wallace, The American mineralogist crystal structure database, Am. Mineral. 88 (2003) 247–250.
[34] A.F. Gualtieri, et al., Quantitative phase analysis using the Rietveld method: towards a procedure for checking the reliability and quality of the results, Period. Mineral. (Aug. 2019), https://doi.org/10.2451/2019PM870.
[35] American National Standards Institute, Measurement of the Leachability of Solidified Low-Level Radioactive Wastes by A Short-Term Test Procedure (ANSI/ANS-16.1-2019), Feb. 22, 2019.
[36] J. Liu, J.-H. Doh, D.E.L. Ong, Z. Liu, M.N.S. Hadi, Methods to evaluate and quantify the geopolymerization reactivity of waste-derived aluminosilicate precursor in alkali-activated material: a state-of-the-art review, Constr. Build. Mater. 362 (Jan. 2023) 129784, https://doi.org/10.1016/j.conbuildmat.2022.129784.
[37] G.V.P. Bhagath Singh, K.V.L. Subramaniam, Quantitative XRD study of amorphous phase in alkali activated low calcium siliceous fly ash, Constr. Build. Mater. 124 (Oct. 2016) 139–147, https://doi.org/10.1016/j.conbuildmat.2016.07.081.
[38] M. Mahyar, S.T. Erdoğan, Phosphate-activated high-calcium fly ash acid-base cements, Cem. Concr. Compos. 63 (Oct. 2015) 96–103, https://doi.org/10.1016/j.cemconcomp.2015.09.002.
[39] M. Zribi, S. Baklouti, Investigation of Phosphate based geopolymers formation mechanism, J. Non-Cryst. Solids 562 (Jun. 2021) 120777, https://doi.org/10.1016/j.jnoncrysol.2021.120777.
[40] L. Monasterio-Guillot, C. Rodriguez-Navarro, E. Ruiz-Agudo, Kinetics and mechanisms of acid-pH weathering of pyroxenes, G-cubed 22 (11) (Nov. 2021), https://doi.org/10.1029/2021GC009711.
[41] H. Douiri, S. Louati, S. Baklouti, M. Arous, Z. Fakhfakh, Structural, thermal and dielectric properties of phosphoric acid-based geopolymers with different amounts of H3PO4, Mater. Lett. 116 (Feb. 2014) 9–12, https://doi.org/10.1016/j.matlet.2013.10.075.
[42] A. Taherizadeh, et al., Thermochemical study of the structural stability of low-silicate CHA zeolite crystals, Results Chem. 4 (Jan. 2022) 100466, https://doi.org/10.1016/j.rechem.2022.100466.
[43] L. Van Tendeloo, et al., Chabazite: stable cation-exchanger in hyper alkaline concrete pore water, Environ. Sci. Technol. 49 (4) (Feb. 2015) 2358–2365, https://doi.org/10.1021/es505346j.
[44] Po-Ling Liu, G.D. Sherman, L.D. Swindale, Laboratory formation and characterization of taranakite in a hydrol humic latosol soil from Hawaii, Pac. Sci. XX (Oct. 1966). https://core.ac.uk/download/pdf/5097454.pdf.
[45] R. Laviano, S. Fiore, Brushite, hydroxylapatite, and taranakite from Apulian caves (southern Italy): new mineralogical data, Am. Mineral. 76 (Jan. 1991) 1722–1727.
[46] J.N.Y. Djobo, D. Stephan, The reaction of calcium during the formation of metakaolin phosphate geopolymer binder, Cem Concr Res 158 (Aug. 2022) 106840, https://doi.org/10.1016/j.cemconres.2022.106840.
[47] F. Zhao, et al., The influence of composite modification of precursor and activator on the properties of the silica-aluminum phosphate geopolymer, Ceram. Int. 51 (10) (Apr. 2025) 13317–13329, https://doi.org/10.1016/j.ceramint.2025.01.176.
[48] J.N. Yankwa Djobo, R.Y. Nkwaju, Preparation of acid aluminum phosphate solutions for metakaolin phosphate geopolymer binder, RSC Adv. 11 (51) (2021) 32258–32268, https://doi.org/10.1039/D1RA05433C.
[49] C. Li, S. Wang, Y. Wang, X. An, G. Yang, Y. Sun, Study on synergistic leaching of potassium and phosphorus from potassium feldspar and solid waste phosphogypsum via coupling reactions, Chin. J. Chem. Eng. 65 (Jan. 2024) 117–129, https://doi.org/10.1016/j.cjche.2023.06.020.
[50] A. Nana, et al., Comparison of feldspar and meta-halloysite geopolymers by alkaline and acidic activation, Constr. Build. Mater. 424 (Apr. 2024) 135953, https://doi.org/10.1016/j.conbuildmat.2024.135953.
[51] A. Nana, et al., Comparison of feldspar and meta-halloysite geopolymers by alkaline and acidic activation, Constr. Build. Mater. 424 (Apr. 2024) 135953, https://doi.org/10.1016/j.conbuildmat.2024.135953.
[52] M. Nanthini, R. Ganesan, V. Jaganathan, Incorporation of nanoalumina in potassium feldspar-based phosphoric acid activated geopolymer composites: a sustainable approach, Journal of Environmental Nanotechnology 13 (3) (Sep. 2024) 89–98, https://doi.org/10.13074/jent.2024.09.243840.
[53] A. Seidel, Y. Zimmels, Mechanism and kinetics of aluminum and iron leaching from coal fly ash by sulfuric acid, Chem. Eng. Sci. 53 (22) (Nov. 1998) 3835–3852, https://doi.org/10.1016/S0009-2509(98)00201-2.
[54] A. Tang, L. Su, C. Li, W. Wei, Effect of mechanical activation on acid-leaching of kaolin residue, Appl. Clay Sci. 48 (3) (Apr. 2010) 296–299, https://doi.org/10.1016/j.clay.2010.01.019.
[55] L. Cui, Y. Guo, X. Wang, Z. Du, F. Cheng, Dissolution kinetics of aluminum and iron from coal mining waste by hydrochloric acid, Chin. J. Chem. Eng. 23 (3) (Mar. 2015) 590–596, https://doi.org/10.1016/j.cjche.2014.05.017.
[56] M. Bu, Q. Yang, P. Wang, B. Dong, D. Hou, Y. Wang, Dissolution behaviors and mechanisms of metakaolin in acidic activators, Cem Concr Res 178 (Apr. 2024) 107442, https://doi.org/10.1016/j.cemconres.2024.107442.
[57] C.-Y. Zhang, et al., Description of Si and Al Release from Aluminosilicate in the Acidic Condition Using Density Functional Theory: protonated Terminal Oxygen, Sustainability 14 (21) (Nov. 2022) 14390, https://doi.org/10.3390/su142114390.
[58] Q. Wan, R. Zhang, Y. Zhang, Structure and properties of phosphate-based geopolymer synthesized with the spent fluid catalytic-cracking (SFCC) catalyst, Gels 8 (2) (Feb. 2022) 130, https://doi.org/10.3390/gels8020130.
[59] Z. Yang, et al., Effects of magnesia and borax on the compressive strength and microstructure of phosphoric acid-activated metakaolin geopolymer, Appl. Clay Sci. 252 (May 2024) 107344, https://doi.org/10.1016/j.clay.2024.107344.
[60] M. Zribi, B. Samet, S. Baklouti, Effect of curing temperature on the synthesis, structure and mechanical properties of phosphate-based geopolymers, J. Non-Cryst. Solids 511 (May 2019) 62–67, https://doi.org/10.1016/j.jnoncrysol.2019.01.032.
[61] A. Nikolov, Novel one-part ferro-phosphate geopolymer cement, Rev. Bulg. Geol. Soc. 81 (3) (Dec. 2020) 43–45 [Online]. Available: https://hal.science/hal-04494184.
[62] A.R. de Carvalho, B.R. da S. Calderón-Morales, J.C. Borba Júnior, T.M. de Oliveira, G.J.B. Silva, Proposition of geopolymers obtained through the acid activation of iron ore tailings with phosphoric acid, Constr. Build. Mater. 403 (Nov. 2023) 133078, https://doi.org/10.1016/j.conbuildmat.2023.133078.
[63] Z. Xu, C. Li, X. Peng, Immobilization of radioactive borate liquid waste using calcined laterite–phosphoric acid–Fe3O4-based geopolymer waste forms, Ceram. Int. 50 (22) (Nov. 2024) 48164–48173, https://doi.org/10.1016/j.ceramint.2024.09.166.

[64] J.N.Y. Djobo, D. Stephan, A. Elimbi, Setting and hardening behavior of volcanic ash phosphate cement, J. Build. Eng. 31 (Sep. 2020) 101427, https://doi.org/10.1016/j.jobe.2020.101427.
[65] R.A. Hernández Hernández, Kaolin bleaching by leaching using phosphoric acid solutions, J. Mex. Chem. Soc. 59 (3) (Oct. 2017), https://doi.org/10.29356/jmcs.v59i3.35.
[66] C. Maqueda, J.L.P. Rodríguez, A. Justo, Problems in the dissolution of silicates by acid mixtures, Analyst 111 (9) (1986) 1107–1108, https://doi.org/10.1039/AN9861101107.
[67] G.C. Kennedy, The hydrothermal solubility of silica, Econ. Geol. 39 (1) (Jan. 1944) 25–36, https://doi.org/10.2113/gsecongeo.39.1.25.
[68] V. Mathivet, et al., Acid-based geopolymers: understanding of the structural evolutions during consolidation and after thermal treatments, J. Non-Cryst. Solids 512 (May 2019) 90–97, https://doi.org/10.1016/j.jnoncrysol.2019.02.025.
[69] Z. Ma, et al., Long-term dissolution behavior of amorphous aluminosilicate in sodium hydroxide solution for geopolymer synthesis using circulating fluidized bed combustion fly ash, Constr. Build. Mater. 394 (Aug. 2023) 132143, https://doi.org/10.1016/j.conbuildmat.2023.132143.
[70] J. Liu, et al., Correlation between dissolubilities of Si, Al, and Fe from aluminosilicate precursor and strength of fly ash-based geopolymer, Constr. Build. Mater. 393 (Aug. 2023) 132107, https://doi.org/10.1016/j.conbuildmat.2023.132107.
[71] J. Archez, R. Farges, A. Gharzouni, S. Rossignol, Influence of the geopolymer formulation on the endogeneous shrinkage, Constr. Build. Mater. 298 (Sep. 2021) 123813, https://doi.org/10.1016/j.conbuildmat.2021.123813.
[72] E. Mukiza, Q.T. Phung, S.C. Seetharam, T.N. Nguyen, C. Bruggeman, G. De Schutter, Recent advances in immobilization of radioactive cesium and strontium-bearing wastes in alkali activated materials – a review, J Environ Manage 370 (Nov. 2024) 122746, https://doi.org/10.1016/j.jenvman.2024.122746.
[73] J.M. Zhou, C. Liu, P.M. Huang, Perturbation of taranakite formation by ferrous and ferric iron under acidic conditions, Soil Sci. Soc. Am. J. 64 (3) (May 2000) 885–892, https://doi.org/10.2136/sssaj2000.643885x.
[74] L. Zhenyu, et al., Rapid solidification of highly loaded high-level liquid wastes with magnesium phosphate cement, Ceram. Int. 45 (4) (Mar. 2019) 5050–5057, https://doi.org/10.1016/j.ceramint.2018.11.206.
[75] F. Fattori, et al., Radiation stability and durability of magnesium phosphate cement for radioactive reactive metals encapsulation, Prog. Nucl. Energy 177 (Dec. 2024) 105463, https://doi.org/10.1016/j.pnucene.2024.105463.
[76] Ispettorato Nazionale per la Sicurezza Nucleare e la Radioprotezione, GUIDA TECNICA N. 33 - Criteri di sicurezza Nucleare E Radioprotezione per la Gestione Dei Rifiuti Radioattivi, Jan. 2023.
[77] J.G. Jang, S.M. Park, H.K. Lee, Physical barrier effect of geopolymeric waste form on diffusivity of cesium and strontium, J Hazard Mater 318 (Nov. 2016) 339–346, https://doi.org/10.1016/j.jhazmat.2016.07.003.